Turbulent boundary layer under a solitary wave

GIOVANNA VITTORI AND PAOLO BLONDEAUX

Department of Civil, Environmental and Architectural Engineering - University of Genoa,
Via Montallegro 1, 16145 Genova, Italy

The boundary layer generated by the propagation of a solitary wave is investigated by means of direct numerical simulations of continuity and Navier–Stokes equations. The obtained results show that, for small wave amplitudes, the flow regime is laminar. Turbulence appears when the wave amplitude becomes larger than a critical value which depends on the ratio between the boundary-layer thickness and the water depth. Moreover, turbulence is generated only during the decelerating phase, or conversely, turbulence is present only behind the wave crest. Even though the horizontal velocity component far from the bed always moves in the direction of wave propagation, the fluid particle velocity near the bottom reverses direction as the irrotational velocity decelerates. The strength and length of time of flow reversal are affected by turbulence appearance. Also the bed shear stress feels the effects of turbulence presence.

1. Introduction

As sea waves approach the coastline, they encounter decreasing water depths and steepen. Therefore, nonlinear effects become more relevant and, to describe the flow induced by wave propagation, it is necessary to move from a linear Stokes wave theory to the solitary wave model. Because of the assumption of high Reynolds numbers, the flow far from the bottom is usually considered to be irrotational and viscous effects are neglected. To evaluate the bed shear stress induced by the propagation of a solitary wave, which plays an important role in near-bed processes such as wave damping and sediment transport, Liu & Orfilia (2004) and Liu, Park & Cowan (2007) have investigated the flow in the bottom boundary layer generated by the propagation of a solitary wave. They found that, although the horizontal component of the irrotational velocity is always directed in the direction of wave propagation, the fluid velocity inside the bottom boundary layer reverses its direction after the passage of the wave crest, when the external velocity decelerates. Both the analysis and the experimental measurements of Liu *et al.* (2007) show that also the bed shear stress changes its sign during the decelerating phases and it is opposite to the external velocity.

The theoretical treatments of Liu & Orfilia (2004) and Liu *et al.* (2007) as well as those of previous investigators (e.g. Keulegan 1948; Mei 1983) are based on the assumption that the flow regime within the bottom boundary layer remains laminar. However, under field conditions, it is likely that the flow regime becomes turbulent. Liu (2006) determined the boundary-layer structure under arbitrary transient free-surface long waves, considering the turbulent regime, by introducing the Boussinesq assumption and an eddy viscosity which depends on the distance from the bottom. However, velocity measurements and numerical simulations of oscillatory boundary layers show that turbulence dynamics in an unsteady flow is complex.

Costamagna, Vittori & Blondeaux (2003) have shown that the mechanism which produces turbulence in oscillatory flows is similar to that operating in steady flows. Indeed, in the near-wall region, low-speed streaks appear towards the end of the accelerating phases. Then, during the decelerating phases, these low-speed streaks twist, oscillate and eventually break, generating small vortices. Finally, during the early accelerating phase, the small vortices dissipate because of viscous effects and the flow tends to relaminarize. Therefore, it appears that simple turbulence models can provide a description of the gross features of unsteady boundary layers, but fail to provide an accurate description of turbulence dynamics and of the flow field.

There are other mechanisms which can generate turbulence under a solitary wave. Ting (2006, 2008) has shown that under a breaking solitary wave, turbulence is present in the whole water column and characterized by the presence of large-scale oblique vortices similar to the obliquely descending vortices observed by other investigators in the breaker region. Moving towards the bottom, the two-dimensional coherent vortices break up into smaller three-dimensional eddies and give rise to high-frequency velocity fluctuations. In coastal waters, internal solitary waves (ISW) can also give rise to turbulence. Indeed, field measurements (e.g. Klymak & Moum 2003) suggest that the flow field generated by the propagation of an ISW is affected by turbulence generated by the shear instability at the density interface. Moreover, there is evidence of the presence of a local region of separated flow, under the footprint of an ISW propagating in a sheared current, which is susceptible to a global instability mechanism (Bogucki & Redekopp 1999; Carr & Davies 2006).

In the present paper, we perform direct numerical simulations of the unsteady boundary layer generated close to the bottom by the propagation of a free-surface solitary wave and we consider only the turbulence generated by the instability of the boundary layer. The boundary-layer thickness is assumed to be much smaller than both the horizontal length scale of the wave and the water depth. Therefore, a local model is developed which assumes that turbulence structure within the boundary layer is not affected by the slow spatial variations of the external flow.

The procedure used in the rest of the paper is as follows. In the next section, we formulate the problem and summarize the numerical approach used to determine the flow field. In §3, we describe the numerical results. Some conclusions are given in §4 where the possible developments of the work are briefly outlined.

2. The problem and the solution method

A solitary wave of height H_0^* propagates on a constant water depth h_0^* along the X_1^* direction (a star denotes a dimensional quantity). Assuming large values of the Reynolds number of the phenomenon and following Liu, Park & Cowen (2007), the flow field can be split into three regions: a core region, where the flow is irrotational and the fluid behaves like an inviscid fluid, and two boundary layers, where the flow is rotational and viscous effects are important. One boundary layer is located close the the free surface and the other close to the bottom. As discussed in Liu *et al.* (2007), at the leading order of approximation, the surface boundary layer can be neglected since it is much weaker than that located close to the bottom. Here, the flow field induced by the propagation of the solitary wave is studied introducing the following dimensionless variables:

$$ t = \frac{t^* \sqrt{g h_0^*}}{h_0^*}, \quad \boldsymbol{X} = \frac{\boldsymbol{X}^*}{h_0^*}, \quad \zeta = \frac{\zeta^*}{H_0^*}, \quad \boldsymbol{V} = \frac{\boldsymbol{V}^*}{\epsilon \sqrt{g^* h_0^*}}, \qquad (2.1) $$

where t^* indicates the time and $(X_1^*, X_2^*, X_3^*) = X^*$ denote Cartesian coordinates with the X_1^*-axis aligned with the direction of wave propagation and the X_3^*-axis in the vertical direction with the origin at the bottom and pointing upward. Moreover, in (2.1), ζ^* is the free-surface elevation with respect to the still water level, $V = (V_1^*, V_2^*, V_3^*)$ is the velocity and the parameter $\epsilon = H_0^*/h_0^*$ measures the wave amplitude. The scaling quantities used here are different from those employed by Liu *et al.* (2007) and coincide with those adopted by Grimshaw (1971). The main reason to use the same velocity and length scales in the three spatial directions will appear clear later on, when the flow within the bottom boundary layer is considered. Indeed, when turbulence appears, the vertical velocity component is no longer much smaller than the horizontal components and the velocity gradients along the three axes have the same order of magnitude. A further advantage of using the variables defined by (2.1) is the disappearance, both from the problem and from the solution, of the dispersion parameter μ equal to the ratio between the water depth and the length scale of the solitary wave. The reader can easily convert the problem formulated in the following as well as its solution into those obtainable using a conventional length l_0 of the solitary wave as the horizontal length scale and $l_0/\sqrt{g^* h_0^*}$ as the time scale.

Considering large values of the Reynolds number, viscous effects turn out to be negligible except within thin boundary layers and the flow field can be assumed to be irrotational. The solution up to $O(\epsilon^2)$, which provides the free surface and the velocity flow field in the inviscid core region, was obtained by Grimshaw (1971) and is not given herein. The length scale h_0^* introduced in (2.1) is not appropriate for the analysis of the flow within the bottom boundary layer which is characterized by a thickness of order $\delta^* = \sqrt{2\nu^* h_0^*}/\sqrt{g^* h_0^*}$ which is assumed to be much smaller than h_0^*. To determine the flow close to the bottom, let us introduce the new spatial variables,

$$(x_1, x_2, x_3) = (X_1^*, X_2^*, X_3^*)/\delta^* = (X_1, X_2, X_3)/\delta, \qquad (2.2)$$

where $\delta = \delta^*/h_0^*$, and let us denote with (v_1, v_2, v_3) the velocity components within the bottom boundary layer. Then, the problem is posed by continuity and Navier–Stokes equations which, in dimensionless form, are

$$\frac{\partial v_i}{\partial x_i} = 0, \quad \frac{\partial v_i}{\partial t} + \frac{\epsilon}{\delta} v_j \frac{\partial v_i}{\partial x_j} = -\frac{\epsilon}{\delta} \frac{\partial p}{\partial x_i} + \frac{1}{2} \frac{\partial^2 v_i}{\partial x_\ell \partial x_\ell} \quad (i = 1, 2, 3), \qquad (2.3)$$

where use is made of Einstein summation convention and the dimensionless dynamic pressure is introduced $p = p^*/(\epsilon^2 \rho^* g^* h_0^*)$. Moreover, the flow described by (2.3) should match the irrotational flow and satisfy the no-slip condition at the bottom. Far from the bottom, i.e. for x_3 much larger than one, the governing equation in the x_1-direction suggests introducing the modified pressure $\tilde{p}$:

$$\frac{\partial \tilde{p}}{\partial x_1} = \frac{\partial p}{\partial x_1} + \frac{\delta}{\epsilon} \left(\frac{\partial V_1}{\partial t} \right)_{X_3=0}, \qquad (2.4)$$

where $(\partial V_1/\partial t)_{X_3=0}$ can be computed on the basis of the time derivative of the irrotational velocity evaluated at the bottom. From a mathematical point of view, (2.3) requires that δ be of order ϵ, i.e. the ratio ϵ/δ be finite. No practical limitation is given by the above requirement.

Here, to study the flow within the bottom boundary layer and in particular to investigate turbulence structure, the governing equations (2.3) are solved numerically by means of a finite-difference approach in a computational domain of dimensions L_1, L_2 and L_3 in the streamwise, spanwise and vertical directions, respectively.

Appropriate boundary conditions should be forced at the boundaries of the computational domain. At the bottom ($x_3 = 0$), the no-slip condition is forced. Since, for large values of x_3, the flow should tend to the irrotational solution, at $x_3 = L_3$ we force $\partial(v_1, v_2)/\partial x_3 = 0$ and $v_3 = 0$. Of course, L_3 should be sufficiently large to be outside the viscous boundary layer. However, since X_3 is equal to $x_3\delta$ and δ is assumed to be much smaller than one, at $x_3 = L_3$, the vertical velocity component of the outer irrotational solution can still be assumed to vanish. At last, by assuming that h_0^* is much larger than the size of the turbulent eddies which develop within the boundary layer, turbulence structure is assumed to be homogeneous in the streamwise and spanwise directions and periodic boundary conditions are thus forced along the x_1- and x_2-axes. The use of periodic boundary conditions is justified if the computational box is large enough to include the largest eddies, generated by turbulence appearance. Checks on the size of the computational box have been carried out to verify this assumption. The computational mesh is uniform in the streamwise and spanwise directions whereas in the vertical direction a non-uniform mesh has been used to cluster the grid-points close to the bottom where velocity gradients are expected to be larger. The numerical method solves the problem in primitive variables using standard centred second-order finite-difference approximations of the spatial derivatives, whereas the time-advancement of Navier–Stokes equations employs a fractional-step method extensively described by Kim & Moin (1985) and Rai & Moin (1991). Further details on the numerical approach can be found in Vittori & Verzicco (1998).

Since the simulations start when the solitary wave is far from the location where the time development of the boundary layer is computed, vanishing velocity and pressure fields would be the most appropriate initial condition. However, to trigger transition and turbulence appearance, a small (of order 10^{-4}) random, but divergence-free, perturbation is added at the initially vanishing velocity field. This initial perturbation decays and has no effect on the time development of the flow when the flow regime is laminar. On the other hand, in the turbulent regime, different realizations of the velocity field are obtained by repeating the simulations for different initial perturbations. However, the average velocity is unaffected by the changes of the initial perturbation. The phenomenon is simulated considering the passage of just one solitary wave which is sufficient to trigger the appearance of turbulence, when the amplitude of the wave is larger than a critical value.

Before obtaining the results, a set of runs was made to ascertain the reliability and accuracy of the numerical code. In particular, a comparison of the numerical results with the analytical solution of Liu *et al.* (2007) and with their experimental measurements was made. The longitudinal velocity profiles computed along the vertical axis are shown at different wave phases in figure 1 and compared with those evaluated on the basis of Liu *et al.*'s (2007) analysis. The values of the parameters were chosen to reproduce one of the experiments of Liu *et al.* (2007). The results provided by the numerical simulations can be compared with the experimental measurements in figures 8 and 9 of Liu *et al.* (2007) where the theoretical results of Liu *et al.* (2007) are shown together with the laboratory data. The agreement is satisfactory. After the numerical code was tested, further runs were made to select the most appropriate size of the computational box and the number of grid points to be used. The results described so far were obtained for values of the parameters such that the flow regime close to the bottom is laminar. When turbulence is present, it is necessary to verify that the computational box is large enough to include the largest turbulent eddies and the grid size is small enough to describe accurately the dynamics of the smallest ones. In the present problem, it is reasonable to expect that the size of the largest vortical
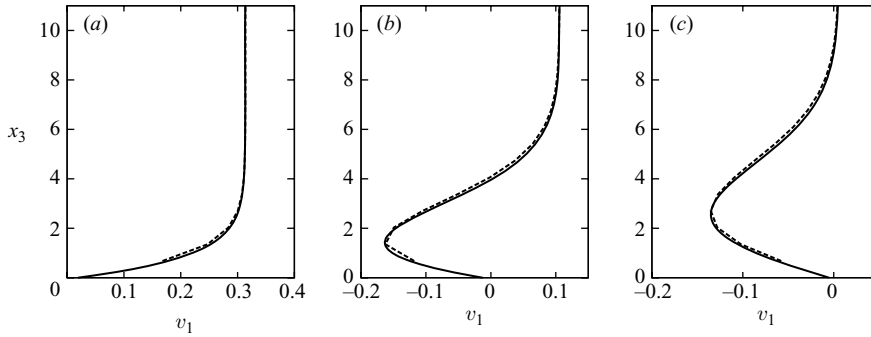
FIGURE 1. Longitudinal velocity component as function of the vertical coordinate at different phases. Solid line, numerical results; broken line, solution by Liu *et al.* (2007). (*a*) $t = 6.94$; (*b*) $t = 14.72$; (*c*) $t = 18.75$. The crest of the solitary wave crosses the measuring section at $t = 10$ ($\epsilon = 0.2$; $\delta = 4.4 \times 10^{-3}$).

structures, which are generated by the intrinsic instability of the boundary layer, are related to δ^*. The work by Costamagna *et al.* (2003), who studied the coherent vortex structures generated in an oscillatory Stokes boundary layer over a flat wall, shows that the largest vortex structures, which appear when transition to turbulence takes place, are vortices elongated in the streamwise direction and characterized by a length of the order of ten times the characteristic thickness of the bottom boundary layer. These considerations gave a first guide to choosing the size of the computational box. The actual dimensions of the box were chosen on the basis of the results provided by a large number of runs which were made also to fix the number of grid points. To give an idea of this preliminary investigation, the runs performed for the case characterized by $\epsilon = 0.5$ and $\delta = 4.75 \times 10^{-4}$ are shown in table 1. The outputs of these preliminary runs were analysed to verify that the averaged quantities and the turbulent vortex structures are unaffected by both the size of the computational box and the number of grid points. Averaged quantities, which are denoted by angle brackets, were evaluated by averaging in the (x_1, x_2)-plane and then averaging the results obtained by means of different numerical simulations obtained for different initial perturbations. Although the smallest box (runs T1, T2) did not allow the free development of the largest vortex structures, the largest boxes (runs T4–T6) allowed the correct development of the largest vortex structures which extract energy from the mean flow and, after the passage of the crest, break up, originating small eddies which then dissipate. This conclusion was confirmed by the analysis of the vorticity fields. To obtain a quantitative measure of the accuracy of the numerical simulations, the auto-correlation of the velocity fluctuations at different phases was computed and it was verified that the numerical box is so large that the fluctuating quantities are uncorrelated for large distances. The number of grid points was chosen in a similar way on the basis of a large number of numerical experiments in order to ensure that even the smallest turbulent eddies are well resolved. This was verified by computing the spectra of the three velocity components along the x_1- and x_3-directions after the passage of the wave crest, at the phases when the strongest turbulent fluctuations and the smaller vortex structures are observed. The results obtained show that the amplitudes of the harmonic components characterized by the highest wavenumbers are practically zero.

Run N	N_1	N_2	N_3	L_1	L_2	L_3
T1	129	120	65	25.13	50	12.57
T2	193	200	97	25.13	50	12.57
T3	193	200	97	25.13	100	50.27
T4	129	100	65	50.27	70	25.13
T5	257	100	129	201.6	70	100.53
T6	385	50	193	150.8	70	75.4

TABLE 1. Numerical simulations carried out to choose the most appropriate size of the computational box and the number of grid points ($\delta = 4.75 \times 10^{-4}$; $\epsilon = 0.5$).
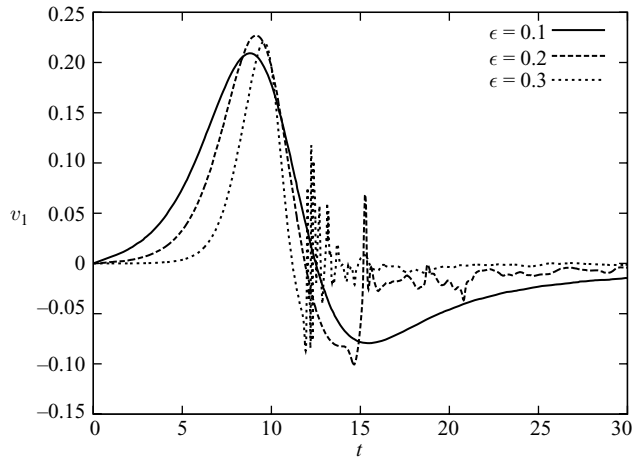

FIGURE 2. Time development of the dimensionless longitudinal velocity component for $\delta = 0.475 \times 10^{-3}$ and $\epsilon = 0.1$ (at $x_3 = 0.34$), $\epsilon = 0.2$ (at $x_3 = 0.34$) and $\epsilon = 0.5$ (at $x_3 = 0.29$). The crest of the solitary wave crosses the measuring section at $t = 10$.

3. Results

The problem is characterized by two dimensionless parameters: ϵ and δ. A large number of runs have been made for different values of ϵ ($0.05 < \epsilon < 0.7$) and δ ($0.282 \times 10^{-4} < \delta < 1.344 \times 10^{-4}$). The flow in the boundary layer at the bottom of a solitary wave can be laminar, transitional or turbulent depending on the values of the parameters and on the wave phase. From the results of figure 2, which shows the time development of the longitudinal velocity component close to the bottom for a constant water depth and waves of different amplitudes, it appears that waves of small amplitude generate a boundary layer which remains laminar. As the amplitude of the wave is increased, a critical value is encountered such that, for larger wave amplitudes, turbulence starts to appear behind the wave crest. Moreover, the turbulent velocity fluctuations become more intense as the wave amplitude increases. When the flow remains laminar, significant negative velocities appear close to the bottom after the passage of the wave crest and they persist for a long time interval. Turbulence increases mixing phenomena and enhances momentum transfer. Hence, the values of the negative velocity decrease when turbulence appears. Moreover, the time interval, during which significant negative values of the velocity are encountered, decreases as ϵ is increased. This finding is confirmed by the streamwise velocity profiles which show that, shortly after the passage of the wave crest, negative values of v_1 are encountered
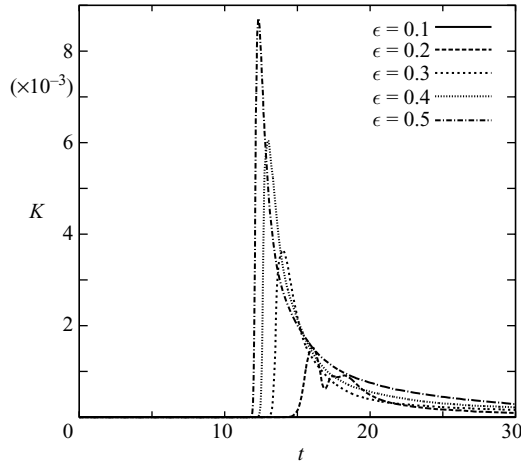
FIGURE 3. Time development of the dimensionless turbulent kinetic energy K per unit area of the bottom for $\delta = 0.475 \times 10^{-3}$. The crest of the solitary wave crosses the measuring section at $t = 10$.

close to the bed. However, the intensity and the time interval during which this flow reversal takes place decrease as ϵ is increased and turbulence appears.

The turbulent velocity fluctuations, which take place at flow reversal in the bottom boundary layer, induce large values of the turbulent kinetic energy as can be seen from figure 3 where the time development of the turbulent kinetic energy K per unit area of the bottom $(K = (1/S) \int_V k \, dV = (1/2S) \int \langle (v_1'^2 + v_2'^2 + v_3'^2) \rangle dV$ where V denotes the volume of the numerical box and S its bottom surface) is shown for different runs which correspond to solitary waves of different amplitudes propagating on the same water depth. In figure 3, the dimensionless turbulent kinetic energy is multiplied by ϵ^2 to account for the scaling introduced by (2.1). It can be seen that K increases abruptly shortly after the passage of the wave crest and then decreases with time. Larger values of ϵ cause an anticipation in the growth of K which reaches higher values. For run $\delta = 0.475 \times 10^{-3}$ and $\epsilon = 0.1$, a vanishing value of K is found, in accordance with the output of the velocity probe which shows the absence of turbulent fluctuations (see figure 2). The vertical profiles of the turbulent kinetic energy $k = \langle (v_1'^2 + v_2'^2 + v_3'^2) \rangle / 2$ at different wave phases (see figure 4) show that the turbulent kinetic energy is suddenly produced close to the bottom after the passage of the wave crest. As time progresses, the energy diffuses in the vertical direction and then the turbulent kinetic energy tends to decay. The explosive generation of turbulent fluctuations after the passage of the wave crest is evident also, considering the time development of the components of the Reynolds stresses. Figure 5 shows the vertical profiles of the largest components of the Reynolds stresses at different wave phases, for $\delta = 0.475 \times 10^{-3}$ and $\epsilon = 0.5$. After the passage of the wave crest, which takes place at $t = 10$, the component $\langle v_1' v_1' \rangle$ starts to grow and attains the largest values close to the bottom while the other components remain negligible (see figure 5a). Later, the component $\langle v_3' v_3' \rangle$ grows and attains values of the same order of magnitude of $\langle v_1' v_1' \rangle$ while the other components still have a smaller amplitude (see figure 5b). At the following phases, the maximum values of the components $\langle v_1' v_1' \rangle$ and $\langle v_3' v_3' \rangle$ decay, even though significant values of $\langle v_1' v_1' \rangle$ and $\langle v_3' v_3' \rangle$ are observed also at large distances from the bottom (see figure 5c). When $\langle v_1' v_1' \rangle$ and $\langle v_3' v_3' \rangle$ start to decay, the other components of the Reynolds stress tensor still grow. Note that these phases
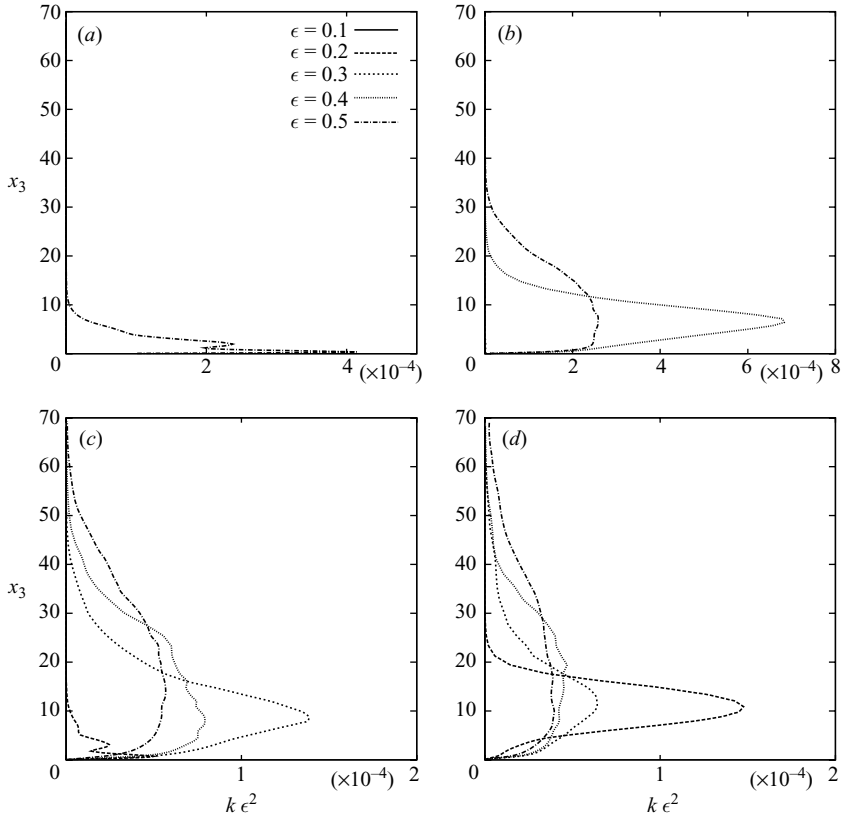
FIGURE 4. Vertical profiles of the dimensionless turbulent kinetic energy k for $\delta = 0.475 \times 10^{-3}$. (*a*) $t = 12.0$; (*b*) $t = 13.0$; (*c*) $t = 15.0$; (*d*) $t = 16.0$. The crest of the solitary wave crosses the measuring section at $t = 10$.

are characterized by large velocity fluctuations (figure 2). Then, all the components of the Reynolds stress tensor decay (see figure 5*d*). Similar results are found for different values of δ, but the critical value of the parameter ϵ above which turbulence appears, increases as δ is increased. In other words, the critical wave amplitude which induces turbulence appearance increases as h_0^* is decreased. The results obtained are summarized in figure 6 where the flow regime in the bottom boundary layer is shown as a function of δ and ϵ. The time development of the bottom shear stress (figure 7), similarly to the velocity, shows a maximum value which is attained slightly before the passage of the wave crest. Moreover, after the passage of the wave crest, the bottom shear stress reverses its direction, being opposite to the direction of wave propagation. As ϵ is increased, the maximum shear stress increases, but high values of the shear stress are restricted to a shorter time interval. Figure 7 shows that, as ϵ is increased, the phase of the maximum shear stress increases slightly and approaches the phase of the maximum water elevation which is coincident with that of the velocity in the irrotational region. In depth-averaged models, the shear stress τ_b^* transmitted by the fluid to the bottom is usually evaluated by means of the Chezy law, and τ_b^* is assumed to be proportional to the square of the irrotational velocity evaluated at the bottom ($\tau_b^* = \rho^* c_f |u_b^*| u_b^*$) (see e.g. El, Grimshaw & Kamchatnov 2007). The results of Liu *et al.* (2007) for the laminar regime and those obtained here for the turbulent
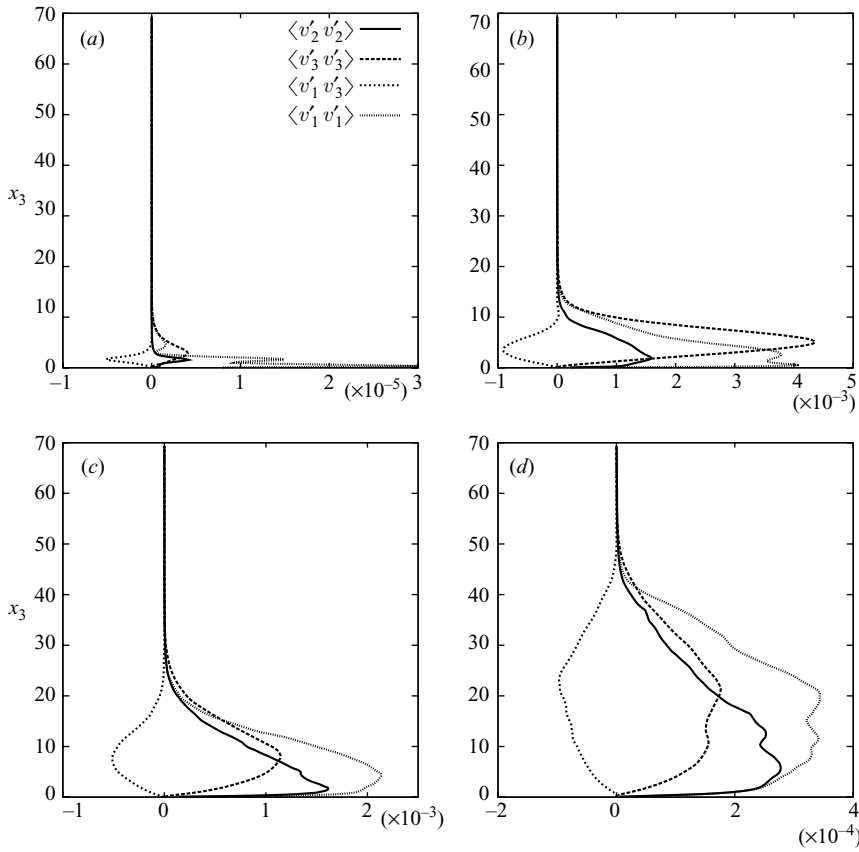
FIGURE 5. Vertical profiles of the largest dimensionless components of the Reynolds stress tensor for $\delta = 0.475 \times 10^{-3}$ and $\epsilon = 0.5$. (a) $t = 11.8$; (b) $t = 12.2$; (c) $t = 12.6$; (d) $t = 14.0$. The crest of the solitary wave crosses the measuring section at $t = 10$.
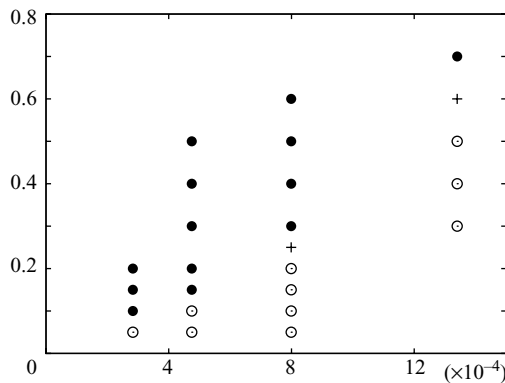

FIGURE 6. Flow regime in the boundary layer at the bottom of a solitary wave as function of δ and ϵ. Laminar regime ($\bigcirc$); transitional regime ($+$); turbulent regime ($\bullet$).

regime show that a phase shift between the maximum of the irrotational velocity and that of the bed shear stress is present. This phase shift is likely to have an influence on many phenomena such as sediment transport in suspension. To improve the predictive capabilities of the depth-averaged models, Liu & Orfilia (2004) and
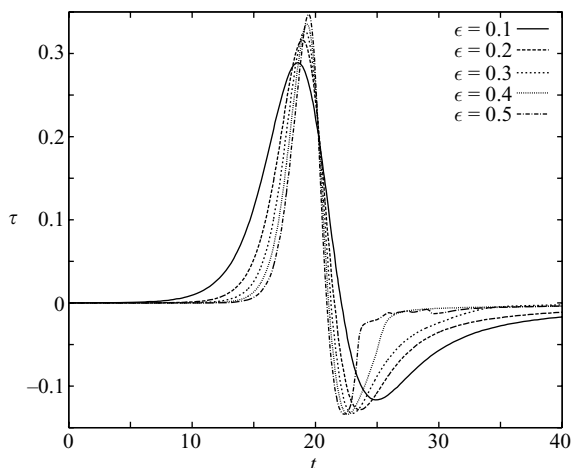
FIGURE 7. Time development of the dimensionless bottom shear stress ($\tau = \tau^*/(\epsilon\rho^* g^* \delta^*)$) for $\delta = 0.475 \times 10^{-3}$. The crest of the solitary wave crosses the measuring section at $t = 20$.

Liu *et al.* (2006) introduced an empirical phase shift between the bottom velocity and the bottom stress. However, the inversion of the direction of the bed shear stress which takes place after the passage of the wave crest, the irrotational velocity being always positive, suggests that a more refined constitutive law should be employed to evaluate the bed shear stress in depth-averaged models.

4. Conclusions

The flow field in the boundary layer at the bottom of a solitary wave is determined by means of numerical simulations of continuity and Navier–Stokes equations. The approach allows the investigation of the turbulent regime which appears, for large wave amplitudes, after the passage of the wave crest when the external flow decelerates. As in the laminar regime, after the passage of the wave crest, the flow in the bottom boundary layer reverses its direction. However, the appearance of turbulence tends to decrease both the strength and the duration of the flow reversal. The improved knowledge of turbulence dynamics should lead to an improvement in the predictions of the wave damping and of the sediment transport rate induced by a solitary wave.

Note added in proof

The numerical results have not been tested against laboratory and/or field data, because of the lack of detailed accurate measurements. When the present paper was in the process of printing, Sumer *et al.* (2008) published experimental measurements of the velocity field in a boundary layer which approximates that generated by a solitary wave. The qualitative agreement between the numerical simulations and the experimental data, which show turbulence fluctuations only during the decelereting phase, supports the present results.

REFERENCES

BOGUCKI, D. J. & REDEKOPP, L. G. 1999 A mechanism for sediment resuspension by internal solitary waves, *Geophys. Res. Lett.* **26**, 1317–1320.

CARR, M. & DAVIES, P. A. 2006 The motion of an internal solitary wave of depression over a fixed bottom boundary in a shallow, two-layer fluid. *Phys. Fluids* **18**, 016601-1–10.

COSTAMAGNA, P., VITTORI, G. & BLONDEAUX, P. 2003 Coherent structures in oscillatory boundary layers. *J. Fluid Mech.* **474**, 1–33.

EL, G. A., GRIMSHAW, R. H. & KAMCHATNOV, A. M. 2007 Evolution of solitary waves and undular bores in shallow-water flows over a gradual slope with bottom friction. *J. Fluid Mech.* **585**, 213–244.

GRIMSHAW, R. 1971 The solitary wave in water of variable depth. Part 2. *J. Fluid Mech.* **46**, 611–622.

KEULEGAN, G. H. 1948 Gradual damping of solitary wave. *J. Res. Natl Bur. Stand.* **40**, 607–614.

KIM, J. & MOIN, P. 1985 Application of a fractional-step method to incompressible Navier–Stokes equations. *J. Comput. Phys.* **59**, 308–323.

KLYMAK, J. M. & MOUM, J. N. 2003 Internal solitary waves of elevation advancing on a shoaling shelf. *Geophys. Res. Lett.* **30**, doi:10,1029/2003GL017706.

LIU, P. L. 2006 Turbulent boundary layer effects on transient wave propagation in shallow water. *Proc. R. Soc. Lond.* A **462**, 3481–3491.

LIU, P. L. & ORFILIA, A. 2004 Viscous effects on transient long-wave propagation. *J. Fluid Mech.* **520**, 83–92.

LIU, P. L., SIMARRO, G., VANDEVER, J. & ORFILIA, A. 2006 Experimental and numerical investigation of viscous effects on solitary wave propagation in a wave tank. *Coastal Engng* **53**, 181–190.

LIU, P. L., PARK, Y. S. & COWEN, E. A. 2007 Boundary layer flow and bed shear stress under a solitary wave. *J. Fluid Mech.* **574**, 449–463.

MEI, C. C. 1983 *The Applied Dynamics of Ocean Surface Waves.* John Wiley.

RAI, M. M. & MOIN, P. 1991 Direct simulations of turbulent flow using finite-difference schemes. *J. Comput. Phys.* **96**, 15–53.

SUMER, B. M., JENSEN, P. M., SORENSEN, L. B., FREDSOE, J. & LIU, P. L. F. 2008 Turbulent solitary wave boundary layer. *Proc. 18th Intl Offshore and Polar Engineering Conf.*, pp. 775–781. International Society of Offshore and Polar Engineers (ISOPE).

TING, F. C. K. 2006 Large scale turbulence under a solitary wave. *Coastal Engng* **53**, 441–462.

TING, F. C. K. 2008 Large scale turbulence under a solitary wave: Part 2. Forms and evolution of coherent structures *Coastal Engng* **55**, 522–536.

VITTORI, G. & VERZICCO, R. 1998 Direct simulation of transition in an oscillatory boundary layer. *J. Fluid Mech.* **371**, 207–232.